High Order Numerical Simulation of Sound Generated by the Kirchhoff Vortex

Bernhard Müller[a] *, **H. C. Yee**[b]

[a] Department of Scientific Computing, Information Technology, Uppsala University, P.O. Box 120, S-751 04 Uppsala, Sweden. (http://www.tdb.uu.se/~bernd/)
[b] NASA Ames Research Center, Moffett Field CA 94035, USA.

Received: January 2001 / Accepted:

Communicated by: A.Quarteroni

Abstract. An improved high order finite difference method for low Mach number computational aeroacoustics (CAA) is described. The improvements involve the conditioning of the Euler equations in perturbation form to minimize numerical cancellation error, and the use of a stable non-dissipative sixth-order central spatial differencing for the interior points and third-order at the boundary points. The spatial difference operator satisfies the summation-by-parts property to guarantee strict stability for linear hyperbolic systems. Spurious high frequency oscillations are damped by a third-order characteristic-based filter. The objective of this paper is to apply these improvements in the simulation of sound generated by the Kirchhoff vortex.

1 Introduction

Owing to the high accuracy requirements in the numerical simulation of acoustic waves, efficient high order numerical methods are most sought after in the emerging area of computational aeroacoustics (CAA) [28,30]. It has been shown that for appropriate high order methods, the number of grid points per wavelength can be greatly reduced from that of standard second-order spatial schemes [4]. Low dispersive fourth-order or higher order schemes have been shown to be the methods of choice for linear or weakly nonlinear aeroacoustics in general geometries. Complex and CPU intensive schemes such as the fifth or higher-order WENO schemes are generally considered as the method of choice if complex nonlinear aeroacoustic problems are involved. The present study is the first of a series of papers [17,18] in an attempt to combine several of the new developments [25,5,27,3,19, 23,22,31–33] in efficient, highly parallelizable high order non-dissipative spatial schemes with characteristic-based filters for CAA that exhibit good long wave propagation accuracy for linear and nonlinear problems [33]. These papers extend the work of [31–33] for CAA. The goal is to propose a scheme that minimizes numerical cancellation errors, and improves nonlinear stability and accuracy associated with low Mach number CAA. These papers utilize the aforementioned new developments in an incremental fashion in order to validate the final approach.

The final form of our scheme consists of two levels. From the governing equation level, we condition the Euler equations in two steps. The first step is to split the inviscid flux derivatives into a conservative and a non-conservative portion that satisfies a so-called generalized energy estimate [3,23]. This involves the symmetrization of the Euler equations via a transformation of variables that are functions of the physical entropy [7]. This splitting of the flux derivatives, hereafter, is referred to as the entropy splitting. The split form of the the Euler equations was found to require less numerical dissipation than its un-split counterpart in association with non-dissipative spatial central schemes [32,33]. Owing to the large disparity of acoustic and stagnation quantities in low Mach number aeroacoustics, the second step is to reformulate the split Euler equations in perturbation form with the new unknowns as the small changes of the conservative variables with respect to their large stagnation values [25]. Nonlinearities and the conservative portion of the split flux derivatives are retained. This perturbation form was shown to minimize numerical cancellation errors compared to the original conservation laws [25].

From the numerical scheme level, a stable sixth-order central interior scheme with a third-order boundary scheme that satisfies the discrete analogue of the integration-by-parts procedure used in the continuous energy estimate (summation-by-parts property (SBP)) is employed [27]. The discrete scalar product is based on a diagonal matrix. If the split form of the inviscid flux derivatives are

* Research support for the first author by TFR, the Swedish Research Council for Engineering Sciences under the project: Numerical Simulation of Vortex Sound; part of the research was conducted as a visiting scientist at RIACS, NASA Ames Research Center.

not used, only linear stability is retained. Characteristic and nonreflecting boundary conditions (BCs), if needed, are imposed at each time step. To suppress the spurious high frequency oscillations associated with central schemes, a modified version of the characteristic-based filter method of Yee et al. [31] is used. The metric terms in the general coordinate transformation are discretized by the same difference operator as the flow variables leading to freestream preservation (uniform flow conservation) [29] for the conservative portion of the split equations. The time derivative is approximated by a 4-stage low-storage second-order explicit Runge-Kutta method with careful treatment of the intermediate BC at the different stages of the Runge-Kutta method to minimize loss of time accuracy [2,4,10].

The numerical experiments presented in this paper consider only the perturbation form of the Euler equations. Numerical results to gain nonlinear stability (and further minimize the use of numerical dissipation) via the entropy splitting will be presented in [17,18].

The numerical method has been applied to the computation of vortex sound. The prediction of vortex sound has been one of the most important goals in computational aeroacoustics (CAA), because the noise in turbulent flow is generated by vortices. To verify the high order finite difference method for the 2D Euler equations, here, we focus on the numerical simulation of a single Kirchhoff vortex. The Kirchhoff vortex is an elliptical patch of constant vorticity rotating with constant angular frequency in irrotational flow. The acoustic pressure generated by the Kirchhoff vortex is governed by the 2D Helmholtz equation, which can be solved analytically using separation of variables [16]. The sound generated by the Kirchhoff vortex constitutes a new challenging test case for CAA. It allows to check numerical methods for the Euler equations on 2D polar grids and to test boundary conditions at the surface of a sound generator and at the farfield.

The outline of the paper is as follows. The perturbation formulation of the Euler equations [25] is reviewed in Section 2. The summation-by-parts (SBP) finite difference operator is reviewed in Section 3. The analytical solution for the sound generated by the Kirchhoff vortex is described in Section 4. Numerical results are compared with the analytical solution in Section 5.

2 Perturbation Formulation of the Euler Equations

In low Mach number aeroacoustics, the changes in pressure, density, etc. are much smaller than their reference values. For example, the acoustic pressure p' is usually many orders of magnitude lower than the stagnation pressure p_0. Computing small differences of large numbers on the computer leads to cancellation. The perturbation formulation introduced in [25] is used to minimize numerical cancellation error for compressible low Mach number flow. The Euler equations are expressed in terms of the changes of the flow variables with respect to their stagnation values. Since the velocity in stagnant flow is zero and the stagnation conditions are constant, the Euler equations in perturbation form can be written as

$$\frac{\partial \rho'}{\partial t} + \nabla \cdot (\rho \mathbf{u})' = 0\,, \tag{1}$$

$$\frac{\partial (\rho \mathbf{u})'}{\partial t} + \nabla \cdot (\rho \mathbf{u})' \mathbf{u}' + \nabla p' = 0\,, \tag{2}$$

$$\frac{\partial (\rho E)'}{\partial t} + \nabla \cdot ((\rho H)' \mathbf{u}' + (\rho H)_0 \mathbf{u}') = 0\,, \tag{3}$$

where

$$\rho' = \rho - \rho_0, \qquad (\rho \mathbf{u})' = \rho \mathbf{u}, \qquad (\rho E)' = \rho E - (\rho E)_0\,,$$

$$\mathbf{u}' = \frac{(\rho \mathbf{u})'}{\rho_0 + \rho'}, \qquad p' = (\gamma - 1)[(\rho E)' - \frac{1}{2}(\rho \mathbf{u})' \cdot \mathbf{u}'],$$

$$(\rho H)' = (\rho E)' + p'.$$

Here, ρ denotes the density, $\mathbf{u}$ the velocity, E the total energy per unit mass, H the total enthalpy, and $\gamma = 1.4$ the ratio of specific heats for air at standard conditions. The "$\prime$" and subscript "0" denote perturbation and stagnation variables, respectively.

Although the present formulation is mathematically identical with the conventional conservative form, discretizing e.g. ∇p leads to cancellation errors, whereas these errors are avoided when discretizing $\nabla p'$. In Cartesian coordinates, the perturbed 2D Euler equations can be expressed as

$$\frac{\partial \mathbf{U}'}{\partial t} + \frac{\partial \mathbf{F}_1'}{\partial x} + \frac{\partial \mathbf{F}_2'}{\partial y} = 0\,, \tag{4}$$

where

$$\mathbf{U}' = \begin{pmatrix} \rho' \\ (\rho u)' \\ (\rho v)' \\ (\rho E)' \end{pmatrix}, \quad \mathbf{F}_1' = \begin{pmatrix} (\rho u)' \\ (\rho u)' u' + p' \\ (\rho v)' u' \\ (\rho H)' u' + (\rho H)_0 u' \end{pmatrix},$$

$$\mathbf{F}_2' = \begin{pmatrix} (\rho v)' \\ (\rho u)' v' \\ (\rho v)' v' + p' \\ (\rho H)' v' + (\rho H)_0 v' \end{pmatrix}.$$

Here, $u' = u$ is the x-direction velocity and $v' = v$ is the y-direction velocity.

For the treatment of general geometries, a coordinate transformation $(x(\xi,\eta), y(\xi,\eta))$ is used. The resulting transformed 2D Euler equations are

$$\frac{\partial \hat{\mathbf{U}}'}{\partial t} + \frac{\partial \hat{\mathbf{F}}_1'}{\partial \xi} + \frac{\partial \hat{\mathbf{F}}_2'}{\partial \eta} = 0\,, \tag{5}$$

where

$$\hat{\mathbf{U}}' = J^{-1}\mathbf{U}'\,,$$
$$\hat{\mathbf{F}}_1' = J^{-1}\xi_x \mathbf{F}_1' + J^{-1}\xi_y \mathbf{F}_2'\,,$$
$$\hat{\mathbf{F}}_2' = J^{-1}\eta_x \mathbf{F}_1' + J^{-1}\eta_y \mathbf{F}_2'\,,$$

with the Jacobian determinant of the transformation $J^{-1} = \frac{\partial x}{\partial \xi}\frac{\partial y}{\partial \eta} - \frac{\partial x}{\partial \eta}\frac{\partial y}{\partial \xi}$, and the metric terms

$$J^{-1}\xi_x = \frac{\partial y}{\partial \eta}\,, \quad J^{-1}\xi_y = -\frac{\partial x}{\partial \eta}\,,$$
$$J^{-1}\eta_x = -\frac{\partial y}{\partial \xi}\,, \quad J^{-1}\eta_y = \frac{\partial x}{\partial \xi}\,.$$

3 Numerical Method

3.1 Summation-by-Parts (SBP) Operator

For linear partial differential equations, well-posedness of the Cauchy problem or initial-boundary-value problems (IBVPs) can be proved by the energy method [12,5]. The essential mathematical tool in the energy method for continuous problems is integration-by-parts

$$(u, v_x) = u(1)^T v(1) - u(0)^T v(0) - (u_x, v)\,. \tag{6}$$

Here u and v are differentiable d-dimensional real functions on $[0,1]$ and not to confuse with the u and v velocities of the 2D Euler equations. The $(u,v) = \int_0^1 u^T v\, dx$ is the L_2 scalar product and $||u||^2 = (u,u)$ denote the L_2 norm.

As an example, we consider the scalar linear advection equation

$$u_t + cu_x = 0\,, \qquad 0 \le x \le 1\,, \tag{7}$$

$$u(x,0) = f(x)\,, \qquad 0 \le x \le 1\,, \tag{8}$$

$$u(0,t) = g(t)\,, \qquad 0 \le t\,, \tag{9}$$

where the wave speed $c > 0$ is constant. Application of the product rule and (6) to (7), we obtain the equalities

$$\frac{d}{dx}||u(\cdot,t)||^2 = 2(u,u_t) = -2c(u,u_x)$$
$$= -c(u^2(1,t) - u^2(0,t)) = -cu^2(1,t) + cg^2(t)\,. \tag{10}$$

Note that $u^T = u$ for the scalar problem (7). Integration over a time interval $[0,t]$ shows that the energy $\frac{1}{2}||u(\cdot,t)||^2$ can be estimated in terms of the initial condition (IC) and BCs. Thus, the problem is well-posed.

For the moment, let's discretized the computational domain $[0,1]$ by $N+1$ grid points $x_j = jh$, $j = 0,1,...,N$, with $h = \frac{1}{N}$. Denote $v_j = v_j(t)$ and $w_j = w_j(t)$ as the approximations of $u(x_j,t)$ and $\frac{\partial}{\partial x}u(x_j,t)$, respectively, and $v = [v_0, v_1, ..., v_N]^T$ and $w = [w_0, w_1, ..., w_N]^T$. Kreiss and Scherer [13], Strand [27] and Carpenter et al. [1] constructed high order difference operators Q for

$$w = Qv \tag{11}$$

such that the summation-by-parts (SBP) property is satisfied, i.e.

$$(u, Qv)_h = u_N v_N - u_0 v_0 - (Qu, v)_h\,, \tag{12}$$

where $u, v \in \mathbb{R}^{N+1}$. The discrete scalar product and norm are defined by

$$(u,v)_h = hu^T H v \qquad ||u||_h^2 = (u,u)_h\,,$$

where H is a symmetric positive definite $(N+1)\times(N+1)$ matrix.

We employ the SBP operator, which is third-order accurate near the boundary and compatible with the standard sixth-order central difference operator in the interior. It was derived by Strand [27] and is of the form

$$(Q_x v)_j = \begin{cases} \frac{1}{h}\sum_{k=0}^{8} d_{jk} v_k & ,j = 0,...,5, \\ (Q_x^{(6)} v)_j & ,j = 6,...,N-6, \\ -\frac{1}{h}\sum_{k=0}^{8} d_{N-j,k} v_{N-k} & ,j = N-5,...,N, \end{cases} \tag{13}$$

where $(Q_x^{(6)}v)_j = \frac{1}{h}(\frac{1}{60}v_{j+3} - \frac{3}{20}v_{j+2} + \frac{3}{4}v_{j+1} - \frac{3}{4}v_{j-1} + \frac{3}{20}v_{j-2} - \frac{1}{60}v_{j-3})$ is the standard sixth-order central difference approximation of the first derivative. The forms of the 5×9 matrix $D = (d_{jk})$ and matrix H can be found in [27,3]. Here H is the diagonal matrix defining the norm of the SBP operator. Since the SBP operator (13) is based on a diagonal norm, its application to multi-dimensions is straightforward.

To closely maintain the order of accuracy of the scheme in curvilinear coordinates, the metric terms are discretized by the same difference operators as the flux derivatives in (5). We approximate the ξ-derivatives $\frac{\partial}{\partial \xi}$ by the SBP operator Q_ξ (13) and the η-derivatives $\frac{\partial}{\partial \eta}$ by the standard sixth-order central difference operator $Q_\eta^{(6)}$. In 3D, the Vinokur and Yee [29] treatment of the corresponding metric terms for freestream preservation is recommended.

In order to not destroy the SBP property, there are different ways in imposing the physical BCs in conjunction with the SBP operator to obtain strict linear stability [1,20,21]. The penalty method called "simultaneous approximation term" (SAT) of Carpenter et al. [1] or the projection method of Olsson [20,21] are two popular SBP preservation approaches. Either approach yields a discrete energy relation similar to the continuous energy relation. Nonlinear stability can be achieved by applying the boundary schemes to the in-going characteristic variables via the entropy splitting form of the inviscid flux derivatives. For simplicity, we have implemented the ingoing Riemann invariants without the SAT or the projection operator. We use instead the so-called injection method, i.e. by imposing them explicitly (cf. section 5) which might destroy the SBP property.

3.2 Time Integration

The application of the spatial discretization of the perturbed Euler equations in transformed coordinates (5) results in a semi-discrete system of nonlinear ODEs

$$\frac{d\mathbf{U}}{dt} = \mathbf{R}(\mathbf{U})\,, \tag{14}$$

where $\mathbf{U}$ is the vector of the difference approximations $\mathbf{U}'_{j,k}$ and $\mathbf{R}$ is the vector of two-dimensional spatial difference operators operating on $\frac{\partial \hat{\mathbf{F}}'_1}{\partial \xi}$ and $\frac{\partial \hat{\mathbf{F}}'_2}{\partial \eta}$ with each element $\mathbf{R}_{j,k} = -J_{j,k}\left[Q_\xi \hat{\mathbf{F}}'_1 + Q_\eta \hat{\mathbf{F}}'_2\right]_{j,k}$.

For efficiency, the ODE system is solved by a multistage method [9]

$$\begin{aligned} \mathbf{U}^{(1)} &= \mathbf{U}^n + \tfrac{\Delta t}{4}\mathbf{R}(\mathbf{U}^n)\,, \\ \mathbf{U}^{(2)} &= \mathbf{U}^n + \tfrac{\Delta t}{3}\mathbf{R}(\mathbf{U}^{(1)})\,, \\ \mathbf{U}^{(3)} &= \mathbf{U}^n + \tfrac{\Delta t}{2}\mathbf{R}(\mathbf{U}^{(2)})\,, \\ \mathbf{U}^{n+1} &= \mathbf{U}^n + \Delta t\,\mathbf{R}(\mathbf{U}^{(3)})\,. \end{aligned} \tag{15}$$

This time discretization is of $O(\Delta t^2)$ for nonlinear problems and $O(\Delta t^4)$ for linear problems. It has the same stability domain as the classical fourth-order Runge-Kutta

method. The CFL conditions for the numerical solution of $\frac{\partial u}{\partial t} + c\frac{\partial u}{\partial x} = 0$, $c = constant$, with periodic IC and BC are (e.g. [15]):
$\sigma \leq 2.828$ for $Q_x^{(2)}$, $\sigma \leq 2.061$ for $Q_x^{(4)}$, $\sigma \leq 1.783$ for $Q_x^{(6)}$, where $\sigma = \frac{c\Delta t}{\Delta x}$ is the CFL number and $Q_x^{(l)}$ denotes the standard central lth-order finite difference method. The difference in the phase errors between the two Runge-Kutta methods will be addressed in a forthcoming paper.

If Dirichlet BCs are properly treated in time, the stability limit for a SBP operator with $Q_x^{(l)}$ in the interior applied to an IBVP will in general be the same as for $Q_x^{(l)}$ applied to a periodic problem, cf. [4], pp. 202-203. However, since the boundary values of time dependent Dirichlet BCs lack the 'errors' expected during the different stages of the classical Runge-Kutta method, the mismatches ruin the normal cancellation of errors to final 4th-order accuracy. Instead, the mismatches lead to $\mathcal{O}(\Delta t)$ and $\mathcal{O}(\Delta x)$ at the boundary and $\mathcal{O}(\Delta x^2)$ globally independent of the high order finite difference operator used. The problem and remedies are discussed in [2,4, 10]. Here, we choose the remedy by, at every intermediate stages of the Runge-Kutta method, the SBP difference operator is also employed at the boundary. After the completion of the full step of the Runge-Kutta method, the Dirichlet BCs are prescribed. Full accuracy in time is achieved using this remedy, but the stability condition becomes more restrictive.

3.3 Characteristic-Based Filter

For long wave propagation of nonlinear systems, even without shock waves and/or steep gradients present, spurious high frequency oscillations are generated by non-dissipative central spatial schemes. To suppress these unresolved waves due to the sixth-order spatial interior scheme, a modified version of Yee et al. [31] high order artificial compressibility method (ACM) filter scheme is used. The ACM filter is based on Harten's ACM [6] switch but utilized in a different context. In the Yee et al. [31,32] schemes, one time step consists of one step with a fourth-order or higher central spatial base scheme. Often an entropy split form of the inviscid flux derivative is used along with a post processing step, where regions of oscillation are detected using the ACM as the sensor, and filtered by adding the numerical dissipation portion of a shock capturing scheme at these parts of the solution. The idea of the scheme is to have the spatially higher non-dissipative scheme activated at all times and to add the full strength, efficient and accurate numerical dissipation only at the shock layers, steep gradients and spurious oscillation parts. Here we employ a similar procedure except we simplified the filter by removing the limiter. Since the present application is for low Mach number CAA, the limiter which is designed for capturing discontinuities is not necessary. Another simplification for low Mach number CAA consists in using the arithmetic average instead of the Roe average.

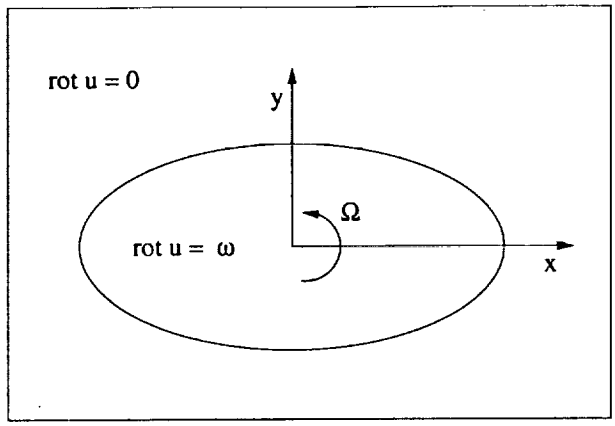

Fig. 1. Kirchhoff vortex.

At the completion of a full step of the Runge-Kutta method, the numerical solution $\mathbf{U}'^{n+1}_{j,k}$ is filtered by

$$\tilde{\mathbf{U}}'^{n+1}_{j,k} = \mathbf{U}'^{n+1}_{j,k} - \Delta t\, J_{j,k}\, [D_\xi \mathbf{U}' + D_\eta \mathbf{U}']^{n+1}_{j,k}\,, \quad (16)$$

where we use the third-order operator

$$D_\xi \mathbf{U}'_{j,k} = \kappa\, \delta_\xi\, \mathbf{R}_\xi\, |\mathbf{\Lambda}_\xi| \delta_\xi^2\, \mathbf{R}_\xi^{-1} \delta_\xi\, \mathbf{U}'_{j,k}$$

with the difference operator $\delta_\xi a_{j,k} = a_{j+1/2,k} - a_{j-1/2,k}$. For our numerical experiments, the filter coefficient κ in the range of $0 \leq \kappa \leq \approx 0.05$ exhibits the desired property. The Jacobian matrix of the flux in the ξ-direction can be diagonalized as $\frac{\partial \hat{\mathbf{F}}_1}{\partial \mathbf{U}} = \mathbf{R}_\xi \mathbf{\Lambda}_\xi \mathbf{R}_\xi^{-1}$.
The columns of $\mathbf{R}_\xi$ are the right eigenvectors of $\frac{\partial \hat{\mathbf{F}}_1}{\partial \mathbf{U}}$ and may be found in [29]. The eigenvalues of $\frac{\partial \hat{\mathbf{F}}_1}{\partial \mathbf{U}}$ define the diagonal matrix $\mathbf{\Lambda}_\xi = diag(u_\xi - c_\xi, u_\xi, u_\xi, u_\xi + c_\xi)$, where $u_\xi = uJ^{-1}\xi_x + vJ^{-1}\xi_y$, and $c_\xi = c\sqrt{(J^{-1}\xi_x)^2 + (J^{-1}\xi_y)^2}$.

$D_\eta \mathbf{U}'_{j,k}$ is defined analogously. Whether a characteristic filter instead of a scalar filter is absolutely necessary will be addressed in a future paper.

4 Analytical Solution for Kirchhoff Vortex Sound

The Kirchhoff vortex is an elliptical patch (Fig. 1) with semi-major axis a and semi-minor axis b of constant vorticity $\nabla \times \mathbf{u} = (0, 0, \omega)^T$ rotating with constant angular frequency $\Omega = \frac{ab}{(a+b)^2}\omega$ in irrotational flow [11]. The 2D flow field constitutes an exact solution of the 2D incompressible Euler equations [14]. The acoustic pressure generated by the Kirchhoff vortex is governed by the 2D Helmholtz equation, which can be solved analytically using separation of variables [16].

The normal velocity for an almost circular Kirchhoff vortex, i.e. $a = R(1+\epsilon)$, $b = R(1-\epsilon)$, $0 < \epsilon \ll 1$, can be approximated by [16]

$$\mathbf{u} \cdot \mathbf{n} \approx 2R\epsilon\Omega\, sin(2(\theta - \Omega t)). \quad (17)$$

Assuming a harmonic time dependence at the angular frequency 2Ω for the acoustic pressure

$$p'(r, \theta, t) = \hat{p}(r, \theta) e^{-i2\Omega t},$$

reduces the wave equation to the Helmholtz equation

$$k^2\hat{p} + \Delta\hat{p} = 0.$$

with wave number $k = 2\Omega/c_0$. Separation of variables yields the solution for the Helmholtz equations

$$p'(r,\theta,t) = \Re(AH_2^{(1)}(kr)e^{i(2(\theta-\Omega t))}), \qquad (18)$$

where $\Re(z)$ denotes the real part of a complex number z. $H_2^{(1)}$ is the Hankel function of 2nd order. The constant

$$A = \frac{\rho_0 4R\epsilon\Omega^2}{kH_2^{(1)\prime}(kR)}$$

is determined by the radial momentum equation

$$\rho_0\frac{\partial u_r}{\partial t} = -\frac{\partial p'}{\partial r}$$

using the normal velocity (17) of the Kirchhoff vortex. In [16], the farfield approximation of (18) for $kr \gg 1$ is shown to coincide with the farfield approximation derived with Green's function [8], pp. 126-128.

An almost circular Kirchhoff vortex generates a similar sound field as an almost circular rotating impermeable ellipse [24].

The exact solution of the 2D linearized Euler equations for sound generated by the Kirchhoff vortex is determined by means of the exact solution of the Helmholtz equation (18). The velocity is computed by

$$\mathbf{u} = \nabla\varphi,$$

where the velocity potential φ is obtained from the relation

$$p' = -\rho_0\frac{\partial\varphi}{\partial t}.$$

Integrating over time and using (18), we get

$$\varphi(r,\theta,t) = -\frac{1}{\rho_0}\int^t p'(r,\theta,\tau)d\tau$$

$$= -\frac{1}{\rho_0}\Re(AH_2^{(1)}(kr)\frac{1}{-2\Omega i}e^{i(2(\theta-\Omega t))}).$$

For isentropic flow, the density perturbation is obtained from

$$\rho' = \frac{1}{c_0^2}p'.$$

5 Numerical examples

In this section we illustrate the accuracy of the high order method by several numerical examples.

5.1 Rotating Kirchhoff Vortex

We consider a Kirchhoff vortex with radius $R = 2m$, $\epsilon = 0.00125$, $\Omega = 82.5\frac{1}{s}$. The stagnation conditions are $\rho_0 = 1.3\frac{kg}{m^3}$, $c_0 = 330\frac{m}{s}$. Thus, the Helmholtz number becomes $\mathcal{H} = kR = 2\Omega R/c_0 = 1$.

A polar grid of mildly stretched near the Kirchhoff vortex in the radial direction, and uniform in the circumferential direction of 129×24 is used. The periodic BCs in the circumferential direction are implemented by 6 overlapping grid points. The exact solution of the linearized Euler equations (cf. Section 4) is prescribed as the IC. At the circle $r = R$ and at the farfield $r = 64.375m$, characteristic BCs are imposed after the completion of a full step of the Runge-Kutta method. With the density, velocity and pressure non-dimensionalized with reference quantities ρ_0, c_0 and $\rho_0 c_0^2$, respectively, the Riemann invariants can be expressed as $p' - u_n$, $p' - \rho'$, u_t and $p' + u_n$. Here, u_n is the normal velocity and u_t is the tangential velocity. The in-going Riemann invariants are prescribed using the exact solution of the linearized Euler equations, while the outgoing Riemann invariants are taken from the numerical solution computed at the boundary. For example, at $r = R$, if $c \geq u_n > 0$ then $p' - u_n = (p' - u_n)_{computed}$, $p' - \rho' = (p' - \rho')_{exact} = 0$, $u_t = (u_t)_{exact}$ and $p' + u_n = (p' + u_n)_{exact}$. If $-c < u_n \leq 0$, the Riemann invariants for the acoustic waves are unchanged, while those for the entropy and vorticity waves become $p' - \rho' = (p' - \rho')_{computed}$ and $u_t = (u_t)_{computed}$.

At the time $T = 200$ with the non-dimensional time step $\Delta t = 0.15$, the Kirchhoff vortex has rotated $7.5radians$. Figures 2 and 3 show the computed solution along the positive x-axis. The solution without the filter compares well with the exact solution of the linearized Euler equations, except near $x = 5$, where high frequency oscillations are visible. These spurious oscillations are eliminated by applying the characteristic-based filter with $\kappa = 0.025$. The filtered and the exact solutions agree up to plotting accuracy. The error in the acoustic pressure in Fig. 3 illustrates that the high frequency oscillations without filter are indeed eliminated by the filter, except in the vicinity of the boundaries. With larger κ, e.g. $\kappa = 0.05$, the deviations near the boundaries slightly increase. It is noted that while the characteristic length scale was chosen as $L = 1m$ in the computation, we use $R = 2m$ in the plots, i.e. $x = \frac{x^*}{L}$ in the computation, where x^* is the x-coordinate in m, and $x = \frac{x^*}{R}$ in the plots. p in the plots corresponds to the non-dimensional acoustic pressure p'.

5.2 Kirchhoff Vortex Started Instantaneously

In section 5.1, a Kirchhoff vortex rotating forever was considered. In this section, the same problem is computed with the IC of the Kirchhoff vortex starting instantaneously from stagnation conditions. The ICs are $\rho' = u' = v' = p' = 0$, except for the circle $r = R$, where the exact solution of the 2D linearized Euler equations for sound generated by the Kirchhoff vortex of Section 4 is prescribed at $t = 0$. At the circle $r = R$, we use the

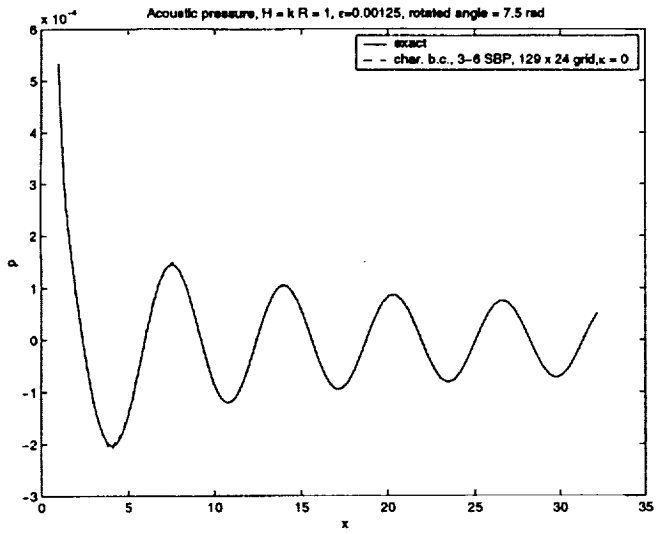

Fig. 2. Comparison of computed and exact acoustic pressure for $\mathcal{H} = 1$, $\epsilon = 0.00125$, rotated angle $= 7.5rad$.

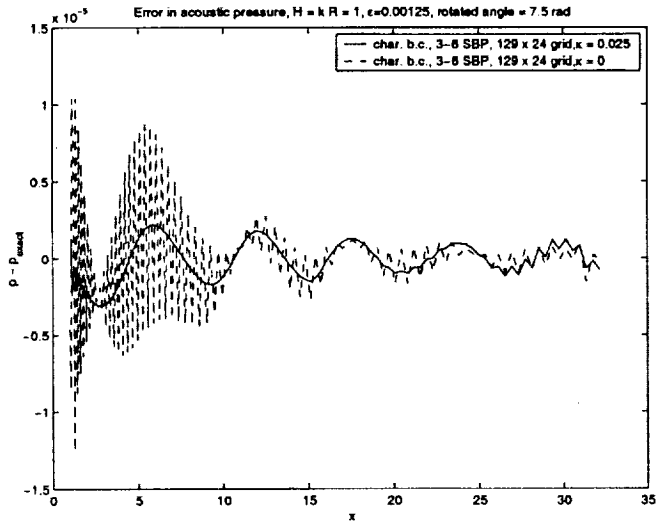

Fig. 3. Influence of filter on error of acoustic pressure for $\mathcal{H} = 1$, $\epsilon = 0.00125$, rotated angle $= 7.5rad$.

same characteristic BCs in Section 5.1. At the farfield, we now use nonreflecting BCs. The implementation procedure is, after the completion of a full step of the Runge-Kutta method, the in-going Riemann invariants for stagnation conditions are prescribed. This means that, at the subsonic farfield boundary $p' - u_n = 0$ is imposed. For $u_n < 0$, $p' - \rho' = 0$ and $u_t = 0$ are imposed as well.

The analytical solution of Section 4 is not valid for the instantaneously started Kirchhoff vortex. It is only valid for a Kirchhoff vortex which has been rotating forever. However, since no wave is travelling from the farfield towards the Kirchhoff vortex, as long as we have stagnation conditions in the farfield, we can assume that the analytical solution for the Kirchhoff vortex rotating for infinitely long time is valid up to the wavefront of the instantaneously started Kirchhoff vortex. If the wavefront has left the domain without reflection at the farfield, the analytical solutions for the instantaneously

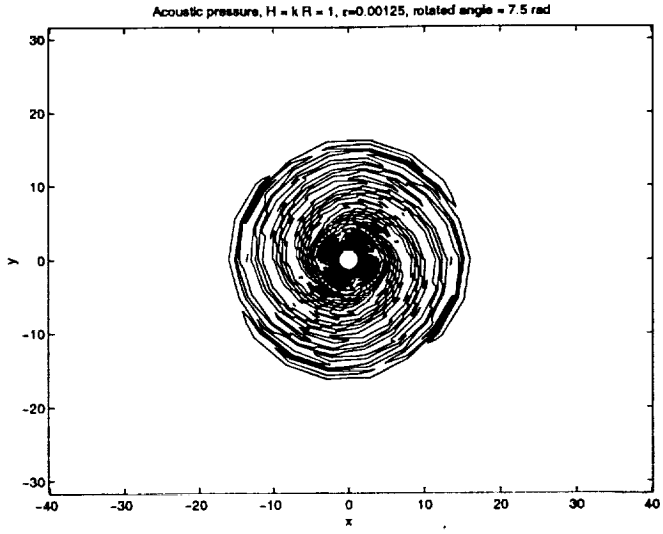

Fig. 4. Acoustic pressure contours without filter for instantaneously started Kirchhoff vortex with $\mathcal{H} = 1$, $\epsilon = 0.00125$, rotated angle $= 7.5rad$.

started Kirchhoff vortex and for the infinitely long rotating Kirchhoff vortex should agree.

Figures 4-6 show the effect of the characteristic-based filter when the wave front has reached $r \approx 16$ (at time $T = 200$, $\Delta t = 0.15$). The numerical solution without filter exhibits spurious oscillations whereas the characteristic-based filter with $\kappa = 0.025$ agrees well with the analytical solution between $r = 1$ and $r \approx 14$. Their difference in accuracy is more apparent from the acoustic pressure shown in Fig. 6 At $x \approx 16$, we see that in general the wavefront cannot match the infinitely long rotating Kirchhoff vortex solution, because the instantaneously started Kirchhoff vortex has zero acoustic pressure downstream of the wavefront. The discrepancies between the numerical solution for the instantaneously started Kirchhoff vortex and the analytical solution for the infinitely long rotating Kirchhoff vortex are therefore, have physical reasons.

Next, we consider the same instantaneously started Kirchhoff vortex as before, but computes for a longer time. After the time reaches 500 (same $\Delta t = 0.15$), the Kirchhoff vortex has rotated 18.75 *radians*. Now, the wavefront is at $r \approx 38.5$. If the wavefront were reflected at the farfield $r = 32.1875$, we should see it at $r \approx 25.875$. The computed acoustic pressure along the positive x-axis shown in Fig. 7 is in excellent agreement with the analytical solution, if the characteristic-based filter with $\kappa = 0.025$ is used. Without the filter, spurious oscillations can be clearly seen. It is interesting to note that even without the filter, the wavefront generated at $t = 0$ by the Kirchhoff vortex has passed through the farfield without visible reflection. The quadrupole structure of the acoustic pressure is correctly recovered by the high order SBP operator with the characteristic-based filter ($\kappa = 0.025$). See Figs. 8 and 9 for the comparison.

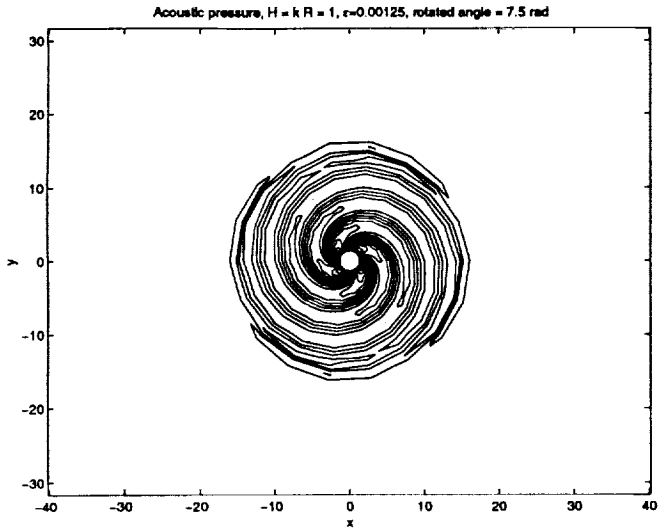

Fig. 5. Acoustic pressure contours with filter for instantaneously started Kirchhoff vortex with $\mathcal{H} = 1$, $\epsilon = 0.00125$, rotated angle $= 7.5rad$.

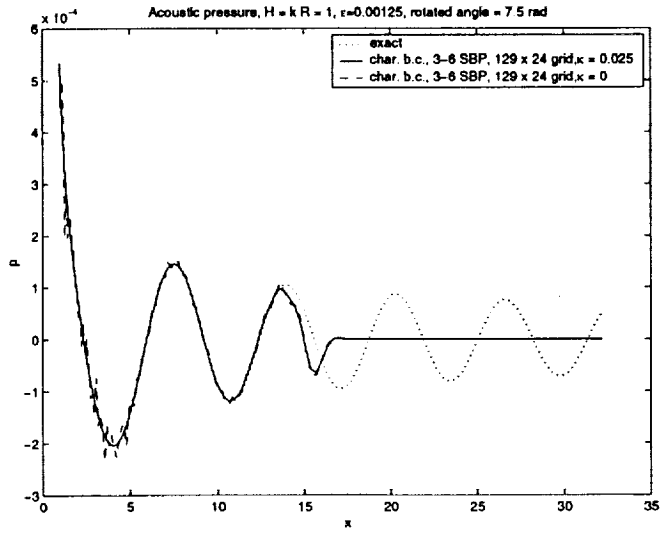

Fig. 6. Comparison of acoustic pressure for instantaneously started Kirchhoff vortex with $\mathcal{H} = 1$, $\epsilon = 0.00125$, rotated angle $= 7.5rad$.

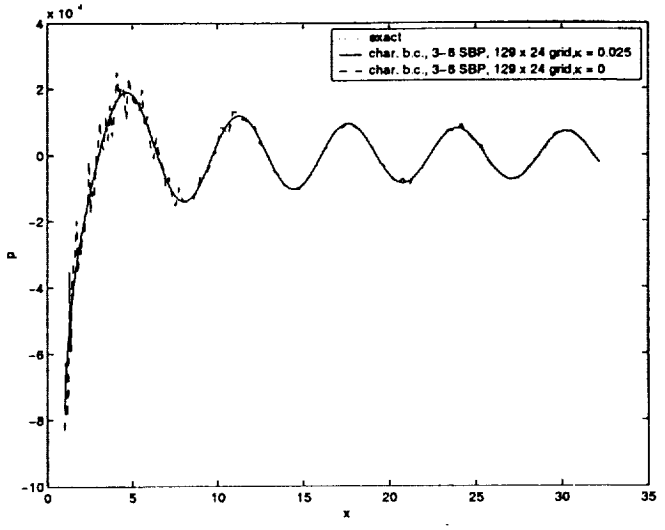

Fig. 7. Comparison of acoustic pressure for instantaneously started Kirchhoff vortex with $\mathcal{H} = 1$, $\epsilon = 0.00125$, rotated angle $= 18.75rad$.

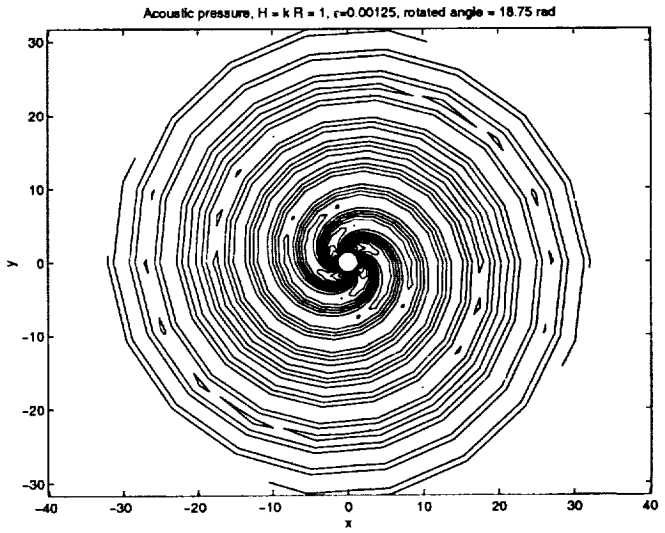

Fig. 8. Acoustic pressure contours with filter for instantaneously started Kirchhoff vortex with $\mathcal{H} = 1$, $\epsilon = 0.00125$, rotated angle $= 18.75rad$.

6 Conclusions

A spatially high order summation-by-parts (SBP) difference operator [27] has been used to solve the 2D Euler equations in perturbation form [25] for the sound generated by the Kirchhoff vortex [16]. For the instantaneously started Kirchhoff vortex, characteristic and non-reflecting BCs are imposed at the completion of each full step of the Runge-Kutta method. Spurious oscillations are eliminated by a characteristic-based filter similar to [31].

In order to gain nonlinear stability for the nonlinear Euler equations in the hope of further minimizing the use of numerical dissipation, future work includes the use of the entropy splitting form of the Euler equations before the application of the perturbation form. The wavelet filter sensors [26] and other possible problem-independent coefficients of the characteristic-based filter will be sought.

References

1. Carpenter, M.H., Gottlieb, D., Abarbanel, S.: Time-Stable Boundary Conditions for Finite-Difference Schemes Solving Hyperbolic Systems: Methodology and Application to High-Order Compact Schemes. J. Comput. Physics, **111**, 220-236 (1994).
2. Carpenter, M.H., Gottlieb, D., Abarbanel, S., Don, W.-S.: The Theoretical Accuracy of Runge-Kutta Time Discretization for the Initial Boundary Value Problem: A Study of the Boundary Error. SIAM J. Sci. Comput., **16**, No. 6, 1241-1252 (1995).

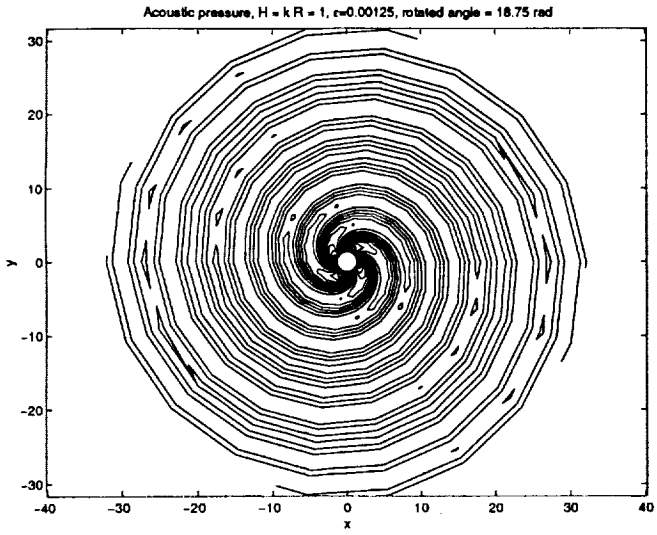

Fig. 9. Exact acoustic pressure contours for Kirchhoff vortex with $\mathcal{H} = 1$, $\epsilon = 0.00125$, rotated angle $= 18.75rad$.

3. Gerritsen, M., Olsson,P.: Designing an Efficient Solution Strategy for Fluid Flows. J. Comput. Physics, **129**, 245-262 (1996).
4. Fornberg, B.: A Practical Guide to Pseudospectral Methods. First Paperback Edition, Cambridge: Cambridge University Press 1998.
5 Gustafsson, B., Kreiss, H.-O., Oliger, J.: Time Dependent Problems and Difference Methods. John Wiley & Sons, New York, 1995.
6. Harten, A.: The Artificial Compression Method for Computation of Shocks and Contact Discontinuities: III. Self-Adjusting Hybrid Schemes, Math. Comp., **32**, 363-389 (1979).
7. Harten, A.: On the Symmetric Form of Systems for Conservation Laws with Entropy. J. Comput. Phys., **49**, 151-164 (1983).
8. Howe, M.S.: Acoustics of Fluid-Structure Interaction. Cambridge: Cambridge University Press 1998.
9. Jameson, A., Baker, T.J.: Solution of the Euler Equations for Complex Configurations. AIAA Paper 83-1929, 1983.
10. Johansson, M.: Loss of High Order Spatial Accuracy due to Boundary Error Caused by Runge-Kutta Time Integration. Technical Report 2000-013, Department of Information Technology, Uppsala University, May 2000. http://www.it.uu.se/research/reports/2000-013/
11. Kirchhoff, G.: Vorlesungen über mathematische Physik. Mechanik. 2nd Edition, Leipzig 1877.
12. Kreiss, H.-O., Lorenz, J.: Initial-Boundary Value Problems and the Navier-Stokes Equation. Academic Press, New York, 1989.
13. Kreiss, H.-O., Scherer, G.: Finite Element and Finite Difference Methods for Hyperbolic Partial Differential Equations. *Mathematical Aspects of Finite Elements in Partial Differential Equations*, Academic Press, New York, 1974.
14. Lamb, H.: Hydrodynamics. 7th Edition, Cambridge University Press, Cambridge, 1975.
15. Lele, S.K.: Compact Finite Difference Schemes with Spectral-like Resolution. J. Comput. Physics, **103**, 16-42 (1992).
16. Müller, B.: On Sound Generation by the Kirchhoff Vortex. Report No. 209/ 1998, Department of Scientific Computing, Uppsala University, October 1998. http://www.tdb.uu.se/archive/reports/report-209-1998.ps.gz
17. Müller, B., Yee, H.C.: Entropy Splitting for High Order Numerical Simulation of Vortex Sound at Low Mach Numbers. RIACS Technical Report, 2001, NASA Ames Research Center
18. Müller, B., Yee, H.C.: High Order Difference Method for Low Mach Number Aeroacoustics. RIACS Technical Report, 2001, NASA Ames Research Center
19. Nordström, J., Carpenter, M.H.: Boundary and Interface Conditions for High-Order Finite-Difference Methods Applied to the Euler and Navier-Stokes Equations. J. Comput. Physics, **148**, 621-645 (1999).
20. Olsson, P.: Summation by Parts, Projections and Stability. I. Math Comp., **64**, No. 211, 1035-1065 (1995).
21. Olsson, P.: Summation by Parts, Projections and Stability. II. Math Comp., **64**, No. 212, 1473-1493 (1995).
22. Olsson, P.: Summation by Parts, Projections and Stability. III. RIACS Technical Report 95.06, 1995.
23. Olsson, P., Oliger, J.: Energy and Maximum Norm Estimates for Nonlinear Conservation Laws. RIACS Technical Report 94.01, 1994.
24. Polifke, W., Paschereit, C.O.: Sound Emissions of Rotor Induced Deformations of Generator Casings. Report, ABB Corporate Research, Baden, Switzerland, 1997.
25. Sesterhenn, J., Müller, B., Thomann, H.: On the Cancellation Problem in Calculating Compressible Low Mach Number Flows. J. Comput. Physics, **151**, 597-615 (1999).
26. Sjögreen, B., Yee, H.C.: Multiresolution Wavelet Based Adaptive Numerical Dissipation Control for Shock-Turbulence Computations. RIACS Technical Report 01.01, October 2000, NASA Ames Research Center.
27. Strand, B.: Summation by Parts for Finite Difference Approximations for d/dx. J. Comput. Physics, **110**, 47-67 (1994).
28. Tam, C.K.W.: Computational Aeroacoustics: Issues and Methods. AIAA J. , **33**, 1788-1796 (1995).
29. Vinokur, M., Yee, H.C.: Extension of Efficient Low Dissipation High Order Schemes for 3-D Curvilinear Moving Grids. NASA TM 209598, 2000, and Proceedings of Computing the Future III: Frontiers in CFD - 2000, Half Moon Bay, CA, June 26-28, 2000.
30. Wells, V.L., Renaut, R.A.: Computing Aerodynamically Generated Noise. Annual Review of Fluid Mechanics, **29**, 161-199 (1997).
31. Yee, H.C., Sandham, N.D., Djomehri, M.J.: Low Dissipative High Order Shock-Capturing Methods Using Characteristic-Based Filters. J. Comput. Physics, **150**, 199-238 (1999).
32. Yee, H.C., Vinokur, M., Djomehri, M.J.: Entropy Splitting and Numerical Dissipation. J. Comput. Physics, **162**, 33-81 (2000).
33. Yee, H.C., Sjögreen, B., Sandham, N.D., Hadjadj, A.: Progress in the Development of a Class of Efficient Low Dissipative High Order Shock-Capturing Methods. RIACS Technical Report 00.01, June, 2000, NASA Ames Research Center; Proceedings of the CFD for the 21st Century, July 15-17, 2000, Kyoto, Japan.